

Retraction

Retracted: Mechanism of Drag Reduction in Floating Plate of Paddy Field Based on CFD

Complexity

Received 19 December 2023; Accepted 19 December 2023; Published 20 December 2023

Copyright © 2023 Complexity. This is an open access article distributed under the Creative Commons Attribution License, which permits unrestricted use, distribution, and reproduction in any medium, provided the original work is properly cited.

This article has been retracted by Hindawi following an investigation undertaken by the publisher [1]. This investigation has uncovered evidence of one or more of the following indicators of systematic manipulation of the publication process:

- (1) Discrepancies in scope
- (2) Discrepancies in the description of the research reported
- (3) Discrepancies between the availability of data and the research described
- (4) Inappropriate citations
- (5) Incoherent, meaningless and/or irrelevant content included in the article
- (6) Manipulated or compromised peer review

The presence of these indicators undermines our confidence in the integrity of the article's content and we cannot, therefore, vouch for its reliability. Please note that this notice is intended solely to alert readers that the content of this article is unreliable. We have not investigated whether authors were aware of or involved in the systematic manipulation of the publication process.

Wiley and Hindawi regrets that the usual quality checks did not identify these issues before publication and have since put additional measures in place to safeguard research integrity.

We wish to credit our own Research Integrity and Research Publishing teams and anonymous and named external researchers and research integrity experts for contributing to this investigation.

The corresponding author, as the representative of all authors, has been given the opportunity to register their agreement or disagreement to this retraction. We have kept a record of any response received.

References

- [1] X. Yu, B. Zhang, and J. You, "Mechanism of Drag Reduction in Floating Plate of Paddy Field Based on CFD," *Complexity*, vol. 2020, Article ID 8852941, 12 pages, 2020.

Research Article

Mechanism of Drag Reduction in Floating Plate of Paddy Field Based on CFD

Xiaoze Yu,¹ Baofeng Zhang,² and Jiahao You³

¹Inner Mongolia University for Nationalities, Tongliao 028000, China

²Yangzhou University, Yangzhou 225127, China

³Jiangsu Shipping College, Nantong 226000, China

Correspondence should be addressed to Jiahao You; 820319927@qq.com

Received 17 September 2020; Revised 17 October 2020; Accepted 26 October 2020; Published 4 December 2020

Academic Editor: Zhihan Lv

Copyright © 2020 Xiaoze Yu et al. This is an open access article distributed under the Creative Commons Attribution License, which permits unrestricted use, distribution, and reproduction in any medium, provided the original work is properly cited.

In order to study drag reduction mechanism in mud parts' operation of surface machine tools for paddy field, this paper takes floating plate, the main working part of laminating mechanism, as the research object and systematically analyzes the mechanism of action of elevation angle, curved angle, penetrating angle, and local microstructure of floating plate on working resistance and local fluid flow characteristics of the laminating structure based on VOF model in Fluent. Using ship mechanics theory and fluid lubrication theory, the drag reduction mechanism under different structural parameters of the floating plate is analyzed. The results show that, compared with the ordinary floating plate, the pressure difference resistance can be reduced by increasing the elevation angle by 60°, curved angle by 20°, and mud separation angle by 20°. The increase of the concave nonsmooth bottom surface structure can reduce viscous frictional resistance, and the total working resistance after structural optimization is comparatively reduced by 48.3%, with lowered hilling height in the forward direction and improved lubrication condition of the bottom surface, forming liquid lubrication effect. This study can provide theoretical references for the optimization design of muddy soil mud parts, mud-machine interaction research, and the development of paddy field laminating mechanism.

1. Instruction

The paddy soil treated by field stepping forms a working layer and a hard underlayer structure, and the working layer is composed of water body and mud. The presence of mud makes the paddy field machine tools bear a large working resistance during the movement. Studies have shown that 40% of the total power consumption of rice transplanters, boat tractors, etc., is used to overcome the mud resistance in the forward process [1]. Therefore, a study on the action law of the machine tool with different surface morphology and structural parameters and paddy mud means great significance for the optimization design of paddy soil mud tools.

In recent years, scholars have carried out abundant experiments and simulation studies on drag reduction mechanism in agricultural machinery. Guo Zhijun et al. studied resistance characteristics of nine bulldozing plate models by the orthogonal test of indoor soil troughs. The

results show that, compared with the traditional curved surface structure, the parabolic bulldozing plate can reduce working resistance by 4.6%, and field mouse claw bionic curved surface structure can reduce the resistance by 16.0% [2]. Under soil moisture content of 20% and with traction resistance and soil adhesion amount as investigation indicators, Tong Jin compared 9 rib-type press rollers, finding that, compared with ordinary press roller, reasonable rib-type press roller has a visbreaking ratio up to 41.08% and a drag reduction rate up to 11.75%~39.4% [3]. Onwualu studied the effect of speed on tillage tool forces by test method and evaluated the experimental results based on three theoretical models. The results show that the second model had a more general agreement with experimental observations [4]. Ucgul et al. simulated interaction between noncohesive soil and plowing machine by EDEM. When soil particle size was 10 mm, the model could accurately predict the traction and vertical force received by the plow in a

certain speed range [5]. Using the discrete element method, JB Barr et al. simulated the effect of opener rake angle on groove profile parameters, ridge height, inclined area, trench backfill, and lateral sling silt of the sandy loam soil and compared the simulation results with the soil trough test. The relative errors were 9%, 16%, 14%, 0.8%, and 9%, respectively [6]. Woodiga and Salazar et al. installed a tail plate behind a generic tractor-trailer truck model to reduce the pressure drag. The effect of the backward-facing step height between the top surface of the trailer and the tail plate on the drag reduction is studied [7]. Skonieczny established the model of soil and farming tools by DEM and showed that excavation forces due to soil accumulation are especially sensitive to cohesion in planetary excavation with various levels of cohesion [8]. Liyan et al. established a soil particle model of paddy field using discrete element software EDEM and designed the mechanical mud parts' surface with a fish scale simulative microstructure. The motion trajectory and different distribution law of mud particles were obtained by numerical simulation, and it was calculated that the total resistance of the bionic sample is 49.84% lower than that of smooth surfaces under paddy soil conditions [9].

In summary, there are many researches on drag reduction mechanism in agricultural machinery at home and abroad, and the application methods are diverse with remarkable results achieved. However, most of them study dry field operation machinery, and there are a few researches on the drag reduction mechanism of paddy field machinery. At the same time, due to the complex fluid characteristics of paddy field mud, the research method for dry field machinery is not applicable to paddy field machinery. Based on the previous studies, this paper analyzes drag reduction mechanism of the floating plate in mud operation and provides a reference for the optimization design of related mud parts, which means great significance for reducing resistance in paddy machinery forward operation and improving the working efficiency of the unit.

2. Physical Model and Numerical Simulation Method

2.1. Physical Model Establishment Method. The actual operation on the paddy field is more complicated; it is a viscous

flow field. For this reason, the physical properties of the paddy field are first considered in the simulation process, and the mud viscosity is measured. The parameters of the mud model are shown in Table 1. The clay viscosity and geometrical characteristics of the floating plate are the most important factors in generating and affecting resistance. When the floating plate travels in the paddy mud at a certain speed, the floating plate is in contact with the mud, causing the local mud to turn, forming a vortex at the head end and the bottom of the floating plate. Moreover, the boundary layer separation occurs and the mud forms a wake flow region in progression at the tail of the floating plate under the extrusion of the floating plate, which causes a pressure change in the pressure field at the tail of the floating plate and results in a pressure difference between the head end and the tail, that is, viscous pressure resistance. Therefore, according to the working characteristics of the laminating mechanism and by virtue of the relative motion principle, the floating plate can be viewed as static, and the mud makes constant turbulence movement relative to the floating plate for numerical simulation. After the mud hits the floating plate, a turbulent flow will form in the floating plate, which is essentially a turbulent process. The mud particles affect each other, while velocity and pressure vary with time and space. Due to the severe turbulence at the head end of the floating plate, the overall flow pattern is considered as a turbulence model according to the definition of classic flow Reynolds number (Re), and wall boundary is selected in the real model. Since there is no heat transfer in the actual operation and energy form is mechanical energy, continuous equation and momentum conservation equation are selected for the governing equation, as shown in equation (1) and equation (2) [10, 11]. Eddy viscosity model is used in the numerical solution process. The standard k-model is used to solve the RANS equation, and RNG k-model with the average strain rate in reaction mainstream is introduced into equation to correct the small vortex in motion [12, 13]:

$$\frac{\partial \rho}{\partial t} + \frac{\partial(\rho u)}{\partial x} + \frac{\partial(\rho v)}{\partial y} + \frac{\partial(\rho w)}{\partial z} = 0, \quad (1)$$

$$\begin{aligned} \frac{\partial(\rho u)}{\partial t} + \frac{\partial(\rho uu)}{\partial x} + \frac{\partial(\rho uv)}{\partial y} + \frac{\partial(\rho uw)}{\partial z} &= \frac{\partial}{\partial x} \left(\mu \frac{\partial u}{\partial x} \right) + \frac{\partial}{\partial y} \left(\mu \frac{\partial u}{\partial y} \right) + \frac{\partial}{\partial z} \left(\mu \frac{\partial u}{\partial z} \right) - \frac{\partial p}{\partial x} + S_u, \\ \frac{\partial(\rho v)}{\partial t} + \frac{\partial(\rho vu)}{\partial x} + \frac{\partial(\rho vv)}{\partial y} + \frac{\partial(\rho vw)}{\partial z} &= \frac{\partial}{\partial x} \left(\mu \frac{\partial v}{\partial x} \right) + \frac{\partial}{\partial y} \left(\mu \frac{\partial v}{\partial y} \right) + \frac{\partial}{\partial z} \left(\mu \frac{\partial v}{\partial z} \right) - \frac{\partial p}{\partial y} + S_v, \\ \frac{\partial(\rho w)}{\partial t} + \frac{\partial(\rho wu)}{\partial x} + \frac{\partial(\rho wv)}{\partial y} + \frac{\partial(\rho ww)}{\partial z} &= \frac{\partial}{\partial x} \left(\mu \frac{\partial w}{\partial x} \right) + \frac{\partial}{\partial y} \left(\mu \frac{\partial w}{\partial y} \right) + \frac{\partial}{\partial z} \left(\mu \frac{\partial w}{\partial z} \right) - \frac{\partial p}{\partial z} + S_w, \end{aligned} \quad (2)$$

TABLE 1: Mud model parameters.

Moisture content (%)	Mud viscosity (Pa·s)	Mud solid phase particle size (μm)	Soil density (g/ml)	Travel speed (m/s)
36.1	4.53	100	2.34	1.44

where S_u , S_v , and S_w are generalized source terms.

2.2. Two-Phase Flow Model Establishment Method. VOF method (Volume of Fluid) determines the free surface tracking fluid change by studying the fluid and mesh volume ratio function in the grid unit [14, 15]. In the solution, the volume fraction of a fluid in a single grid is usually kept updated without changing the interface height in interface tracking. With the advantages of no topological constraints, it is suitable for stratified flow, surface flow, and large bubble flow, thus widely used in multiphase flow models [16]. In the solution process, the volume fraction of liquid in each grid varies from 0 to 1, with 0 representing no such fluid in the grid, 1 representing the liquid filling the grid, and 0.5 representing the interface of the two liquids. The corresponding volume fraction expression is as follows [17, 18]:

$$\frac{\partial \alpha}{\partial t} + \frac{\partial}{\partial x_j} (\alpha u_j) = 0. \quad (3)$$

2.3. Meshing Method. The floating plate model has a complicated structure. In order to eliminate the influence of the grid itself, the same size fluid domain is used to divide the grid, but only local encryption is performed. At the same time, to deal with the interface problem of segmentation interval, workbench is adopted for direct 3D modeling [19, 20]. Wall surface partition and meshing are performed via space claim. Since the model thickness is 10 mm, according to the boundary layer characteristics, to accurately reflect the model features, the inner wall mesh is set to a minimum of 3 layers of mesh, so the grid size of the floating plate is 4 mm, the surrounding of the floating plate is filled with 15 mm grid, and area away from the stamping is set to 25 mm. The mesh generation diagram is shown in Figure 1(a). The maximum number of grids is about 101×10^4 . The model grid computing domain is shown in Figure 1(b).

2.4. Grid Independence Verification. In order to avoid the influence of the size of the grid on the simulation results, four different grid division schemes were selected in turn to verify the grid independence. The model of the stamping board is established by Solidworks. Mesh preprocessing is generated by mesh. High precision grid structured grid and local encryption. The corresponding grid numbers are 851914, 1013400, 1329640, and 1720592 and the entry angle is 50° . Using the grid of fluid motion in the process of membrane plate in contact with soil conditions was analyzed, and the resistance change with iterative is shown. It is seen from Figure 2 when the number of meshes more than 1,013,400, the stable flow field, the calculated resistance is almost the same, the error $< 2\%$. Therefore, the number and

degree of encryption of the mesh calculation are the same as before.

2.5. Boundary Condition Setting and Geometric Model Construction. The floating plate has a movement state in the mud similar to that of the boat in the sea. The common feature of both is that small objects move in a large space. In the calculation domain and initialization model, the distance from the entrance to the model is 5 times that of board length, and the distance from the exit to the model is 3.5 times that of board length. The air zone model has a set height of 1.5 L and a lower water disturbance depth of 400 mm (equal to the board length). The immersion depth is also a value that needs special consideration, which affects the resistance value of the flow process. It can be calculated by the Baker formula, as shown in equations (4) [21, 22]. According to the field operation requirements, the immersion depth of the floating plate is generally 10~30 mm, which is affected by parameters such as mud, transplanting equipment, and degradable film weight. Therefore, the immersion depth is set to 20 mm, which can reflect the resistance value in a larger range:

$$H = \left[\frac{G}{BL(k_c / (B + K_\phi))} \right]^{(1/n)}, \quad (4)$$

where H is the immersion depth of the floating plate, G is the weight of the floating plate (including hydraulic equipment and degradable film), B is the grounding width of the floating plate, L is the grounding length of the floating plate, k_c is the cohesive deformation modulus of the soil, k_ϕ is the soil friction deformation modulus, and n is the soil deformation index.

During the simulation, the position corresponding to the immersion depth is the free interface. According to the VOF model, there is a two-phase flow interface when volume fraction is 0.5, and mud foundation depth is generally 20~40 cm when the paddy field is steeping, so the rationality and accuracy of the simulation can be guaranteed [23, 24]. The free interface height set in this paper is 400 mm and the movement speed of the floating plate is up to 6 km/h. Using a variable reference frame, the mud and air move relative to the floating plate, and the speed at the muddy water inlet and air inlet is set to 1.44 m/s. At the same time, to save the grid, both the floating plate and the air domain adopt symmetric boundaries. The remaining boundary conditions are set as follows:

- (1) The air and muddy water inlets are velocity inlets with a speed of 1.44 m/s.
- (2) The outlet is a restricted pressure outlet.
- (3) There are four wall surfaces, the rear sidewall surface, the bottom wall surface, the upper wall surface, and the wall surface of the floating plate respectively.

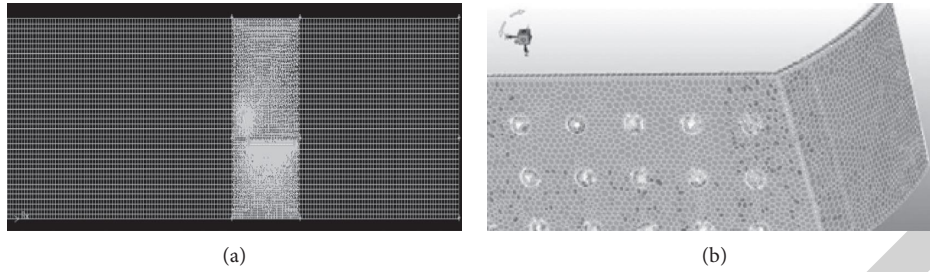


FIGURE 1: Grid division. (a) Mesh generation. (b) Convex hull local mesh refinement.

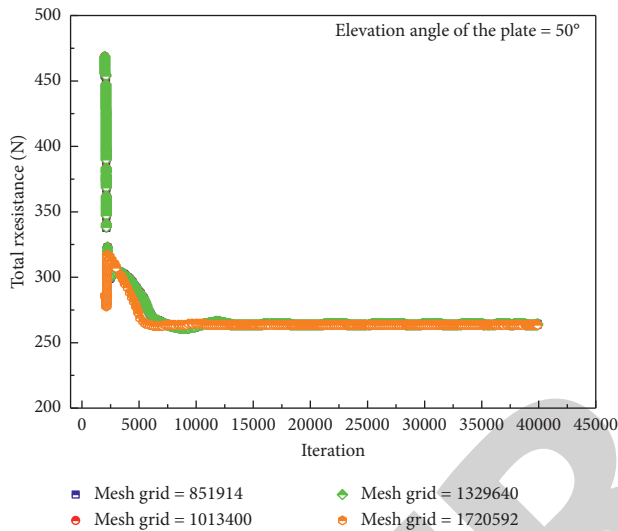


FIGURE 2: Grid independence verification.

- (4) The symmetry boundary is set in a symmetrical boundary condition for free energy and mass transfer.

3. Results and Discussion

Figure 3 shows a dynamic evolution diagram of the volume fraction during the movement of the floating plate. It can be seen from the figure that, with the flow of muddy water, the original static soil begins to move forward, and the soil moving in the horizontal direction hits the bottom of the floating plate. As the floating plate has a certain width and height, after blocked by the floating plate, the muddy water near the bottom of the floating plate is first decelerated, with the velocity dropped to zero. Subjected to inertia and viscosity, the subsequent muddy water cannot be stopped. Therefore, a detour convex hilling is formed at the bottom of the floating plate. Subsequent muddy water cannot continue to move in the horizontal direction, so a detour flow is formed from the bottom and the sides. The height of the hilling will continue to increase for a long time, until the hilling does not rise and stabilizes under the combined effects of gravity, viscous force, and bypass flow on both sides. Due to the influence of gravity during the ascending process of hilling, the angle of the front end boat deck affects

the rising height of the hilling. Therefore, this paper first studies the influence of the angle and height of the boat deck on the hilling height and analyzes the influencing factors affecting hilling and forward resistance.

3.1. Influence of the Front End Angle of the Floating Plate on the Hilling. Because of the space size limit, the floating plate is fixed; a too long length will cause inconvenience. Therefore, in the study of this paper, the floating plate front end length is selected as 160 mm with reference to analyzing the evolution law of hilling height with angle after stabilization. For a too small angle, the floating plate size will be greatly increased, and the too large volume is not conducive to operation. Therefore, the paper studies from the angle which is 35° . It can be seen from Figures 4 and 5 that when the boat deck angle is $35^\circ \sim 50^\circ$, the tilling will flow over the entire front end boat deck. After the angle reaches 60° , tilling is only partially piled up and will not flow over the front end boat deck. This is because, while the muddy water hits the floating plate, the splash height is affected by the angle and height of the front end boat deck of floating plate. The muddy water after the collision will continue to move forward due to inertia, which will produce a significant pressure on the surrounding boat deck.

It can also be seen from the partial pressure cloud map that the pressure here is significantly higher than that in other places, and the pressure will make the muddy water climb along the boat deck. During the climb, the muddy water decelerates and falls under the action of gravity. When the energy for the upward movement is exhausted, hilling will stop. On the one hand, as the angle increases, the component force of gravity increases along the boat deck, which will cause the climbing height to decrease. On the other hand, under the same boat deck length, for a larger angle, the vertical height is higher, the potential energy required for the climb is larger, and the initial kinetic energy is larger. Therefore, there will be a tendency that hilling height decreases with the increase of the angle under the same height of the deck boat.

However, the front end angle of the floating plate is not better as it is higher. From the total resistance variation chart (Figure 6), it can be seen that as the angle increases, the resistance increases and the floating plate travels difficultly. Hence, a lower angle should be selected for an appropriate length. It can be seen from the volume fraction cloud diagram that when the angle is less than 60° , the boat deck will

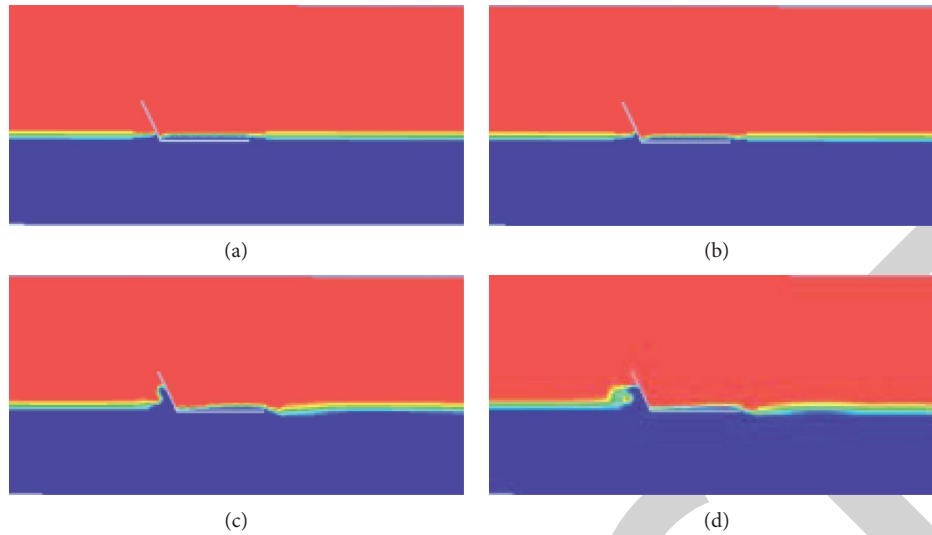


FIGURE 3: 65° floating plate simulation results: (a) 0 s, (b) 0.5 s, (c) 0.1 s, and (d) 2 s.



FIGURE 4: Simulation results of 50° floating plate. (a) 50° free waveform diagram. (b) 50° volume fraction diagram.



FIGURE 5: Simulation results of 60° floating plate. (a) 60° free waveform diagram. (b) 60° volume fraction diagram.

be submerged, and the hilling will turn over the floating plate, which is unfavorable for operation. Nevertheless, when the angle is greater than 60°, the hilling will not turn over the boat deck. Therefore, the angle should be 60° in the design and this angle is maintained for subsequent designs. It can be seen from the simulation results that the resistance of the floating plate is divided into differential pressure resistance and frictional resistance. Due to the high viscosity muddy water characteristics, the differential pressure resistance is slightly larger than the frictional resistance. It can be known from classical fluid mechanics that viscous resistance is directly related to the contact area, so reducing the contact area may be an effective factor for lower total resistance; the front end bottom of the floating plate is subjected to a large pressure, so optimization on it can reduce

the differential pressure resistance, thus overall reducing travel resistance of the floating plate and improving the working efficiency of the laminating machine.

3.2. Influence of the Curved Angle of the Floating Plate on the Hilling Effect. The influence of different curved angle on the resistance of the floating plate is studied by ship theory. The angle range is 5~20°. Figure 7 shows a variation chart of the floating plate resistance under different curved angles. It can be seen from the figure that the frictional resistance basically does not change with the increase of the curved angle, while differential pressure resistance is significantly reduced. Compared with an ordinary floating plate of 0°, the total resistance is reduced by about 11.90~18.18%, where the

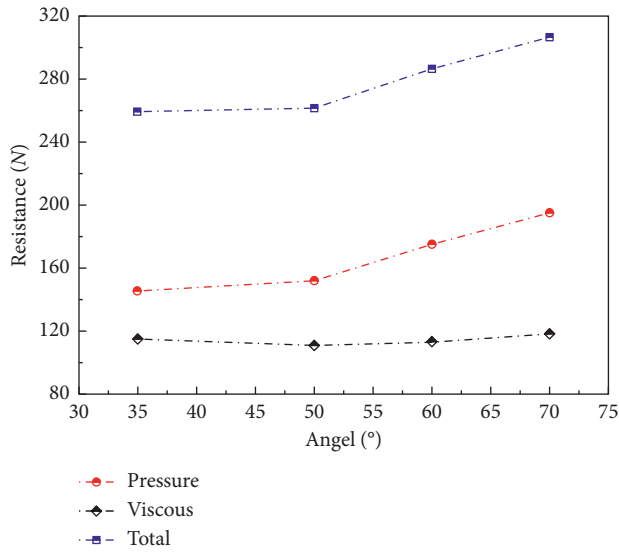


FIGURE 6: Total resistance variation chart.

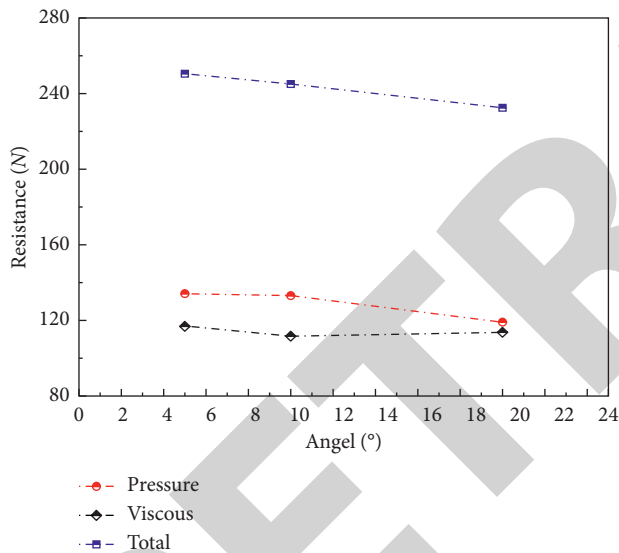


FIGURE 7: Resistance variation chart.

differential pressure resistance is significantly reduced when the curved angle is 20° . It can be seen from the static pressure diagram (Figure 8) that the front end boat deck of the floating plate has a big pressure drop, there is a low-pressure zone at the tail end, and the pressure difference between the two becomes pressure drop resistance. The curved surface boat deck increases the local contact area, buffers the local flow field, reduces the local pressure drop, and reduces the resistance. The pressure decrease also causes the lifting height of muddy water to drop. It can be seen from the volume fraction cloud diagram that, compared with Figure 5, the hilling height has decreased significantly, and the vortex caused by the gas-liquid two-phase separation at the edge is reduced.

It should be pointed out that, from the simulation results, it can be seen that the curved floating plate has a significant effect on the hilling effect, although a smaller

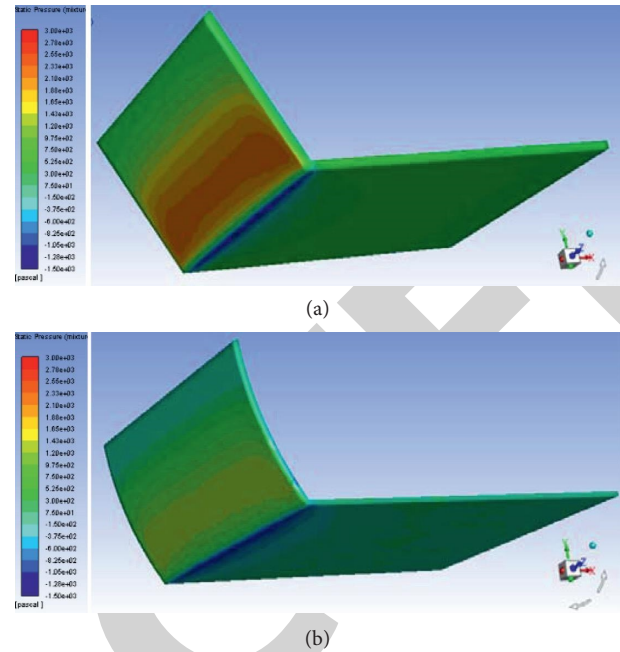


FIGURE 8: Static pressure distribution diagram: (a) static pressure distribution diagram of floating plate and (b) static pressure distribution diagram of floating plate with 20 degrees of curved angle.

angle can play a certain role and the smaller curved angle has little effect on the real situation. Therefore, it is recommended that the surface angle should be designed at around 20° . This is because the resistance will be increased when the angle exceeds a certain value, and at the same time, an excessively large curved surface also increases the cost and difficulty of processing. Excessive annealing will reduce the service life of the floating plate and the floating plate angle should be set to about 20° based on comprehensive consideration.

3.3. Influence of the Penetrating Angle of the Floating Plate on the Hilling Effect. In the ship dynamics, in order to reduce the resistance during the ship movement, the front end of the boat deck is usually in sharp angle to increase the momentum of the ship in the forward direction, breaking the waves and increasing the ship speed [23, 24]. In view of this, a similar penetrating angle of the floating plate structure was designed, and the penetrating angle is in the range of $5^\circ \sim 20^\circ$ considering the paddy field working environment. Figure 9 shows the influence law of different penetrating angles on hilling height above the middle symmetry plane of the floating plate. It can be seen from the figure that hilling height is reduced with the increase of the penetrating angle, and the surface penetrating angle has a significant effect on reducing hilling height. This is because after the muddy water hits the floating plate, under the sharp interface cut, the fluid is easily split and easily flows to both sides. In this way, hilling flows around the floating plate from both sides, thus reducing the forward resistance. At the same time, in the case of a high penetrating angle, it is found that typical

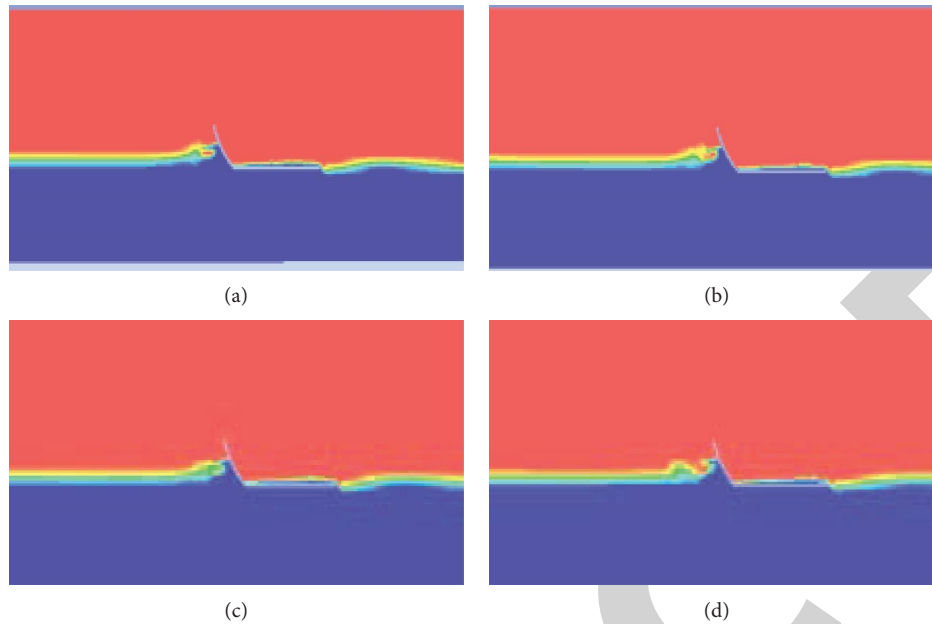


FIGURE 9: Simulation results of different penetrating angle: (a) penetrating angle is 5° , (b) penetrating angle is 10° , (c) penetrating angle is 15° , and (d) penetrating angle is 20° .

hilling is reversed back to the front, and the hilling is completely broken.

It can be seen from the local velocity cloud diagram (Figure 10) that the downward impact speed of the fluid along the floating plate is significantly higher than that of an ordinary floating plate, which also indicates that the floating plate breaks the muddy water on the one hand and accelerates fluid's downward movement on the other hand, thus reducing the hilling height. As can be seen from Figure 11, the pressure difference resistance is maximally reduced by about 21.96% as compared with the maximum of the floating plate without a penetrating angle. The calculation results also show that when the penetrating angle is 5° , great changes occur as compared with ordinary curved surface floating plate, with a drop of about 5.89%, and when the penetrating angle is increased, the effect becomes more and more obvious, but there is abnormal rise when the penetrating angle is 10 degrees, which may be caused by the muddy water break distance at that time.

It can be seen that the viscous resistance does not change basically. It can also be seen from Figure 12 that, with the presence of a penetrating angle, the local maximum pressure distribution changes, which changes from basically uniform distribution to a distribution with the highest static pressure at the position of the penetrating angle. This is consistent with the basic physical common sense, indicating that the result is correct. It is also necessary to point out that the tip of the penetrating angle must be sufficiently strengthened. Otherwise, there will be damage under frequent pressure impact. Therefore, it is recommended to add reinforcing structures such as ribs inside.

3.4. Influence of Local Microstructure of Floating Plate on Resistance. Figure 13 shows the volume fraction cloud diagram of the symmetry plane position. It can be seen from the above

figure that the surface of the three nonsmooth structures does not have a significant effect on the hilling height, but only slight difference exists. It can be seen from the total resistance distribution diagram (Figure 14) that the groove structure resistance has a decrease of 23.05 N compared with the 20° penetrating angle surface, and the concave structure has a decrease of nearly 45 N, while the convex groove structure not only has no resistance drop but instead shows the abnormal phenomenon of increase in resistance. The pressure drop of the three nonsmooth surfaces is basically the same in a detailed analysis, and the convex hull structure has a slight rise, but the rise is not obvious. This is because it can also be seen from the partial pressure cloud diagram of the convex hull structure that the front end facing muddy water of the convex hull structure has a pressure significantly larger than that of the tail. Under the action of a plurality of convex grooves (18), the pressure drop is significantly increased. Although the groove has small increased pressure in the impact surface facing the muddy water, the overall pressure value does not change much. At the same time, it is found that the viscous resistance of the three has a clear difference, the obvious viscous resistance drop of the concave envelope contributes to almost all the resistance drop, indicating that the drag reduction effect is obvious, the viscous resistance of the groove has a slight decline, and the downward trend is not obvious; at the same time, the pressure of the convex hull increases significantly, rising by about 5.2%. Therefore, under the joint action of the two, the resistance of the concave envelope is significantly reduced, while the resistance of the convex hull is significantly increased. The nonsmooth structure at the bottom of the surface primarily reduces the total resistance by reducing the viscous resistance.

Figure 15 is a streamline diagram of three different surfaces. It can be seen from the figure that the flow fields of the three nonsmooth surfaces are completely different. The convex hull surface will show obvious bypass flow

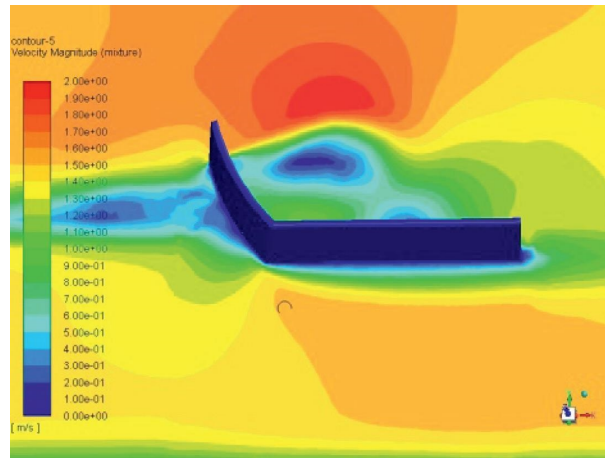


FIGURE 10: Velocity nephogram of 20.

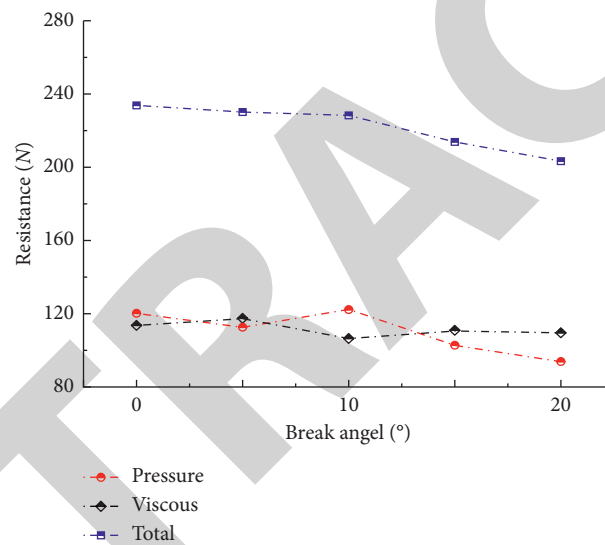
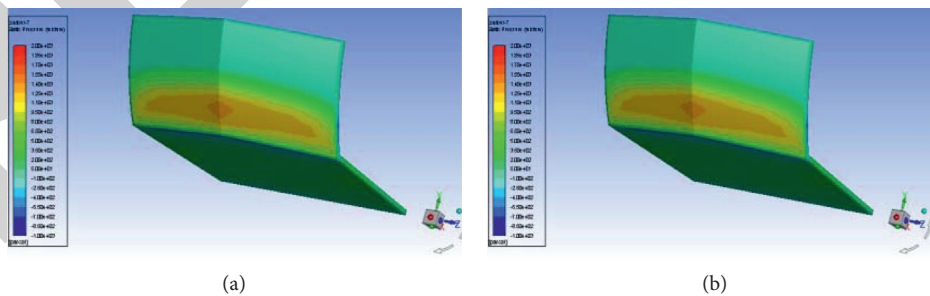


FIGURE 11: Drag distribution picture.

FIGURE 12: Pressure cloud diagram under different penetrating angles: (a) pressure cloud diagram when penetrating angle is 5° and (b) pressure cloud diagram when penetrating angle is 20° .

when hit by the muddy water. A wake flow is formed at the rear after the bypass. Similar to the Carnot vortex, it increases local eddy current, but since there is no local rectification structure, the superimposed disturbance of multiple vortices will inevitably increase the pressure

drop, thereby improving the running resistance. At the same time, the formation of the convex hull increases the contact area of the floating plate at the bottom. For mud flow process with great viscosity, the increase of the contact area means an increase in the viscous resistance,

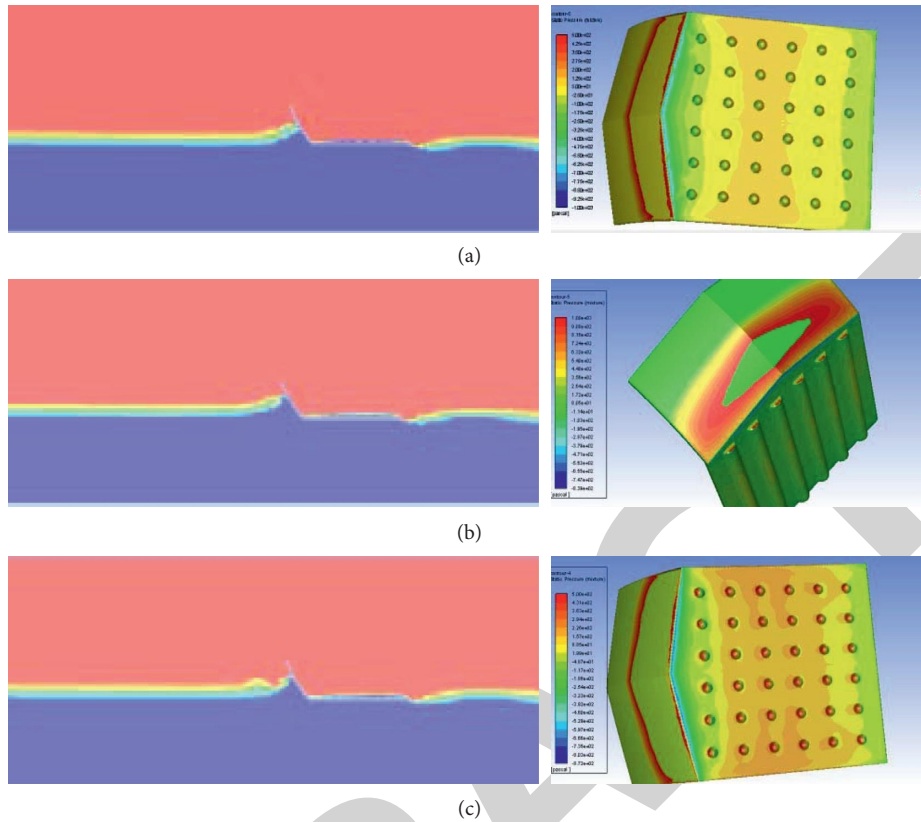


FIGURE 13: Hilling and pressure cloud diagram of nonsmooth bottom: (a) partial hilling and pressure cloud diagram of concave envelop, (b) partial hilling and pressure cloud diagram of groove, and (c) partial hilling and pressure cloud diagram of convex hull.

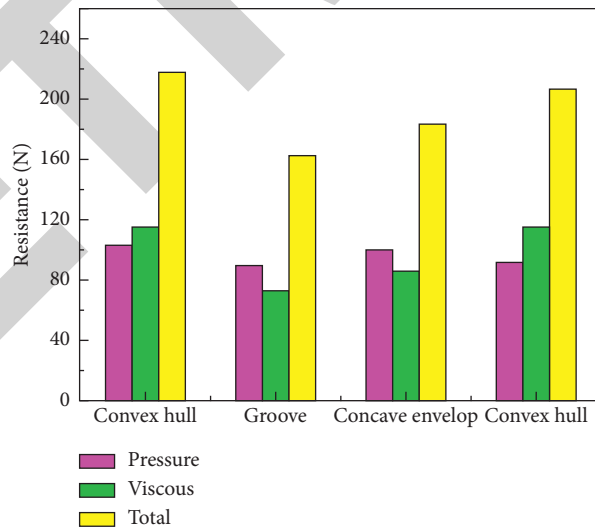


FIGURE 14: Drag distribution picture.

so the overall running resistance of the convex hull increases.

According to the simulation of the groove structure, although the contact area is increased on the surface, since the groove is long, the muddy water moves into the grooves on both sides after the impact, which accelerates the movement in the groove and reduces the viscous resistance.

For the nonsmooth structure of the concave envelope, it can be seen from the local flow field that the flow velocity near the concave envelope is extremely low, and the muddy water almost slips over the concave surface, which means that this is a typical liquid lubrication phenomenon. The muddy water filled in the concave envelope provides a lubricating effect, so that the muddy water slides down the wall surface

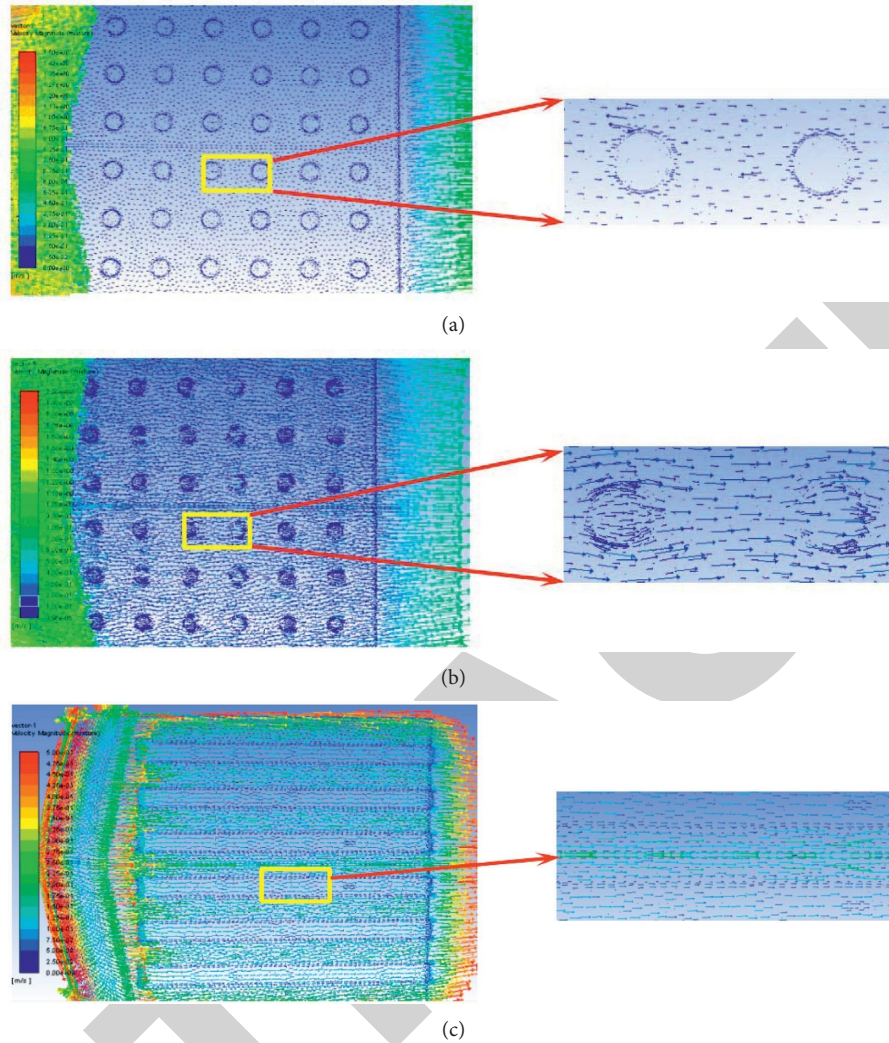


FIGURE 15: Streamline diagram of different bottom structures: (a) Velocity distribution and partial enlargement diagram of concave envelope at 365 mm. (b) Velocity distribution and partial enlargement diagram of convex hull at 365 mm. (c) Velocity distribution and partial enlargement diagram of groove at 365 mm (enlarged as groove superficial zone).

with almost no wall shearing, reducing the overall viscous resistance. Nonsmooth structures are not necessarily conducive to the reduction of total resistance but may also lead to an increase in overall resistance, such as convex hull structure. The reasonable design will reduce the resistance to a certain extent and improve the overall operating efficiency of rice laminating machine, such as concave envelope structure. In summary, we obtained the optimal design parameters for laminating machine under high viscosity in this study. The boat deck angle is 60° , the curved surface radian is 20° , the penetrating angle is 20° , and the bottom is in concave envelope structure.

4. Experimental Verification

In order to verify the accuracy of the simulation results, this paper measures the resistance of different structures of floating plate in the indoor soil trough as Figure 16 shows. The main types of equipment for the test included

electric tractor, suspension mechanism, MIK-LCS1 tension-compression sensor, paddy soil, and floating plate model. Other types of equipment included ruler, stopwatch, marking pen, soil moisture detector, insulating tape, and assembly tools (wrench, screwdriver, plier, etc.).

During the test, the three models were moved from one end of the soil tank at a constant speed, and the moving distance was 1.5 m. Observe and measure the depth of the model sinking into the mud. After moving the model to 1.5 m, we observe the front, back, and two sides of the model, then record the measured results, and smooth the mud surface. Each model was repeated three times, and the results were averaged.

4.1. Test Results. Table 2 shows the traction resistance values measured after different optimization mechanism parameters. It can be seen from the table that the traction resistance

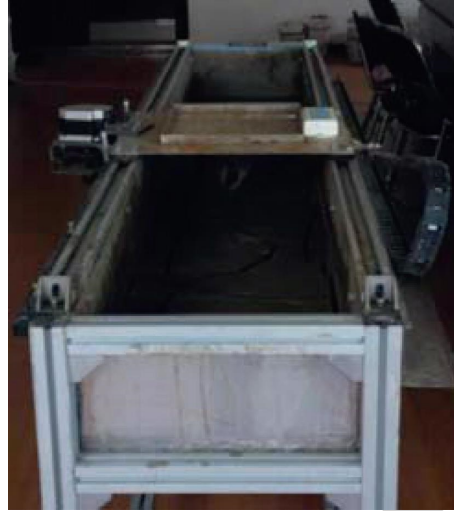


FIGURE 16: The test soil bin.

TABLE 2: Test results of traction resistance of floating plate.

Floating plate structure type	Traction resistance (N)			Average value	Simulation result (N)
	Test value 1	Test value 2	Test value 3		
Common structure	377.3	381.9	351.1	370.1	312.8
Curved structure	284.0	270.1	262.8	272.3	236.2
Penetrating angle structure	240.3	250.5	235.8	245.2	210.0
Baseplate microstructure	203.5	195.6	209.6	202.9	172.7

of the other three improved structures is significantly lower than that of the common structure.

On the basis of the curved structure, the traction resistance is reduced by about 27 N after the addition of the penetrating angle structure. The average traction resistance decreases to 202.9 N after adding the bottom concave envelope microstructure on the basis of the addition of a penetrating angle structure. This shows that, after several structural optimizations, there is a drag reduction effect on the working resistance of the floating plate. At the same time, the relative errors of the simulated and experimental values in the structural resistance of the four types of floating plates were 18.3%, 15.27%, 16.76%, and 17.47%, respectively. In summary, the test results are consistent with the simulation analysis results, and the simulated values are well fitted with the experimental values. Therefore, it is considered that the established interaction model between the mud parts and paddy soil based on the VOF model is reasonable.

5. Conclusion

In this paper, the VOF-coupled level-set model in Fluent is used to systematically study the drag reduction mechanism of the design parameters for the floating plate of the paddy field laminating machine. By investigating the influence mechanism of floating plate angle, curved angle, penetrating angle, and local nonsmooth structure on the running resistance and flow pattern of the floating plate, the research

shows that (1) the angle and height of the floating plate affect the hilling height. Although a smaller angle means small resistance, hilling will easily turn over the boat deck, reducing the effect. Comprehensively considering the hilling effect and resistance, better design angle is 60° under high viscosity; (2) the change of the curved surface shape reduces the pressure difference resistance. Combining theoretical model analysis values, the optimal resistance operation range can be obtained when the floating plate curved angle is 20° ; (3) the increase of the penetrating angle reduces hilling height, lowers running resistance, and improves the operation efficiency. Comprehensively considering local strength, the better design value of penetrating angle is 20° ; (4) the local nonsmooth structure has a significant influence on the viscous resistance. Comparing the three nonsmooth structures, concave envelope has the best drag reduction effect due to the local liquid lubrication. The simulation results were verified through an indoor soil trough test, which realized the innovation of the research method for the drag reduction mechanism of paddy field mud parts. The established model and the data obtained by the simulation result will contribute to the research and optimization design of the drag reduction mechanism of paddy field tools.

Data Availability

The data used to support the findings of this study are included within the article.

Conflicts of Interest

The authors declare that they have no conflicts of interest.

Acknowledgments

This study was supported by the Inner Mongolia National Natural Science Foundation of China (2019LH05002).

References

- [1] S. Karmakar and R. L. Kushwaha, "Dynamic modeling of soil tool interaction: an overview from a fluid flow perspective," *Terramechanics*, vol. 43, no. 3, pp. 411–425, 2005.
- [2] G. Zhijun, D. Gan, Z. Li, and X. Li, "Orthogonal experiment on resistance reduction by soil engaging surfaces of bulldozer blade," *Transactions of the Chinese Society for Agricultural Machinery*, vol. 46, no. 7, pp. 372–378, 2015.
- [3] T. Jin and Z. Qingzhu, "Reduction of soil adhesion and traction resistance of ridged bionic press rollers," *Transactions of the Chinese Society for Agricultural Machinery*, vol. 45, no. 4, pp. 135–140, 2014.
- [4] A. Onwualu, "Draught and vertical forces obtained from dynamic soil cutting by plane tillage tools," *Soil and Tillage Research*, vol. 48, no. 4, pp. 239–253, 1998.
- [5] M. Ucgul, J. M. Fielke, and C. Saunders, "3D DEM tillage simulation: validation of a hysteretic spring (plastic) contact model for a sweep tool operating in a cohesionless soil," *Soil and Tillage Research*, vol. 144, pp. 220–227, 2014.
- [6] J. B. Barr, M. Ucgul, J. M. A. Desbiolles, and J. M. Fielke, "Simulating the effect of rake angle on narrow opener performance with the discrete element method," *Biosystems Engineering*, vol. 171, pp. 1–15, 2018.
- [7] S. Woodiga, D. M. Salazar, P. Wewengkang, J. Montefort, and T. Liu, "Skin-friction topology on tail plate for tractor-trailer truck drag reduction," *Journal of Visualization*, vol. 21, no. 6, pp. 1017–1029, 2018.
- [8] K. Skonieczny, "Modeling the effects of surcharge accumulation on terrestrial and planetary wide-blade soil-tillage tool interactions," *Soil & Tillage Research*, vol. 176, pp. 104–111, 2017.
- [9] W. Liyan, Q. Sheng, T. Q. Song et al., "A DEM analysis on drag reduction characteristics of paddy field machinery surface with bionic microarchitectures," *Journal of Shenyang Agricultural University*, vol. 48, no. 1, pp. 55–62, 2017.
- [10] S. O. Wilson, R. Bryan, R. Pablo, P. I. Monserrate, and S. J. Elizabeth, "Analysis of heat transfer between a coolant fluid and a plastic blowing matrix using the ANSYS CFD tool," in *Proceedings of the World Conference on Information Systems & Technologies*, vol. 746, pp. 280–288, Naples, Italy, May 2018.
- [11] Z. Asaf, D. Rubinstein, and I. Shmulevich, "Determination of discrete element model parameters required for soil tillage," *Soil and Tillage Research*, vol. 92, no. 1–2, pp. 227–242, 2007.
- [12] A. Ibrahim, H. Bentaher, and A. Maalej, "Soil-blade orientation effect on tillage forces determined by 3D finite element models," *Spanish Journal of Agricultural Research*, vol. 12, no. 4, pp. 941–951, 2014.
- [13] P. Busato, "A simulation model for a rice-harvesting chain," *Biosystems Engineering*, vol. 129, pp. 149–159, 2015.
- [14] S. Kawale and V. P. Chandramohan, "CFD simulation of estimating critical shear stress for cleaning flat soiled surface," *Sādhanā*, vol. 42, no. 12, pp. 2137–2145, 2017.
- [15] G. Hoormazdi, J. Küpferle, A. Röttger, W. Theisen, and K. Hackl, "A concept for the estimation of soil-tool abrasive wear using ASTM-G65 test data," *International Journal of Civil Engineering*, vol. 17, no. 1, pp. 103–111, 2019.
- [16] W. Devarrewaere, D. Foqué, B. Nicolai, D. Nuytens, and P. Verboven, "Eulerian-Lagrangian CFD modelling of pesticide dust emissions from maize planters," *Atmospheric Environment*, vol. 184, pp. 304–314, 2018.
- [17] S. E. Gant and H. Tucker, "Computational fluid dynamics (CFD) modelling of atmospheric dispersion for land-use planning around major hazards sites in great Britain," *Journal of Loss Prevention in the Process Industries*, vol. 54, pp. 340–345, 2018.
- [18] W. C. Tyson and C. J. Roy, "A higher-order error estimation framework for finite-volume CFD," *Journal of Computational Physics*, vol. 394, pp. 632–657, 2019.
- [19] Su-D. Kim, J.-Y. Yoon, and S.-J. Na, "A study on the characteristics of FSW tool shapes based on CFD analysis," *Welding in the World*, vol. 62, no. 5, pp. 915–926, 2018.
- [20] A. Janečka, J. Málek, V. Průša, and G. Tierra, "Numerical scheme for simulation of transient flows of non-Newtonian fluids characterised by a non-monotone relation between the symmetric part of the velocity gradient and the Cauchy stress tensor," *Acta Mechanica*, vol. 230, no. 3, pp. 729–747, 2019.
- [21] M. K. Moraveji, M. Sabah, A. Shahryari, and A. Ghaffarkhah, "Investigation of drill pipe rotation effect on cutting transport with aerated mud using CFD approach," *Advanced Powder Technology*, vol. 28, no. 4, pp. 1141–1153, 2017.
- [22] P. Sahoo and A. Sahoo, "Hydrodynamic studies on fluidization of red mud: CFD simulation," *Advanced Powder Technology*, vol. 25, no. 6, pp. 1699–1708, 2014.
- [23] Y. K. Demirel, O. Turan, and A. Incecik, "Predicting the effect of biofouling on ship resistance using CFD," *Applied Ocean Research*, vol. 62, pp. 100–118, 2017.
- [24] M. Haase, K. Zurcher, G. Davidson, J. R. Binns, G. Thomas, and N. Bose, "Novel CFD-based full-scale resistance prediction for large medium-speed catamarans," *Ocean Engineering*, vol. 111, pp. 198–208, 2016.